Uniaxial Optical Phase Change Metamaterials

by

Babatunde Olamide Ogunlade

SUBMITTED TO THE DEPARTMENT OF MATERIALS SCIENCE AND ENGINEERING IN PARTIAL FULFILLMENT OF THE REQUIREMENTS FOR THE DEGREE OF

BACHELOR OF SCIENCE
AT THE
MASSACHUSETTS INSTITUTE OF TECHNOLOGY

JUNE 2020

Signature of Author:_____
Department of Materials Science & Engineering
May 1, 2020

Certified by:_____
Juejun Hu
Associate Professor of Materials Science & and Engineering
Thesis Supervisor

Accepted by:_____
Juejun Hu
Associate Professor of Materials Science & and Engineering
Chairman, Undergraduate Thesis Committee

Uniaxial Optical Phase Change Metamaterials

by

Babatunde Olamide Ogunlade

Submitted to the Department of Materials Science and Engineering on May 1, 2020
In Partial Fulfillment of the Requirements for the Degree of
Bachelor of Science in Materials Science and Engineering

ABSTRACT

Optical metamaterials are artificially engineered materials with exceptional electromagnetic properties that cannot be found in nature. Over the last 20 years, optical metamaterials have driven forward a plethora of fields from telecommunications to solar energy harvesting. They owe their unique optical properties to their carefully arranged subwavelength structural elements. By tuning the shape, geometry, and arrangement of these structures, unconventional optical properties like a negative refractive index can be achieved over a broadband wavelength range of operation. By incorporating optical phase change materials, materials with outstanding optical contrast upon a solid-state phase transition, more control over the optical modulative properties of metamaterials can be achieved. In this paper, $Ge_2Sb_2Te_5$ (GST) is chosen as a model phase change material due to its high reflectance contrast between states, fast switching speeds, and high metastability.

Here, we theoretically investigate the reflectance and form birefringence of GST-based optical metamaterials. These optical properties are simulated on the basis of effective medium theory (EMT) and transfer matrix method (TMM). The findings in this paper demonstrate that broadband wavelength regions of high reflectance, high birefringence, and zero-crossing birefringence can be found and tuned as a function of material thickness and fill fraction in simulated GST-based optical metamaterials. These findings will be valuable for imminent nano and microfabrication in optical devices.

Thesis Supervisor: Juejun Hu
Title: Associate Professor of Materials Science and Engineering

Acknowledgements

I would first like to thank Dr. Christopher Roberts for constantly lending to me his vast expertise and mentorship. Throughout the course of this project, he thoroughly answered any question I had from beginner MATLAB syntax questions to more complex questions about the future of metamaterials with immense patience. During the thesis writing process, he also provided me valuable comments and proofreading.

I would like to thank Professor Hu for his guidance as well. He gave me the opportunity to jump into the field of photonics, a field that I had no previous experience in but was ecstatic to explore nonetheless. I would also like to thank Dr. Carlos A. Ríos Ocampo and Yifei Zhang of the Hu Group for teaching me about phase change materials during the early days of this project.

Finally, I would like to thank all my friends and family for all of their emotional support. To the Logs and B2, thank you for being my people, my home away from home. To Mom, Dad, and Damola, thank you for your unwavering love and motivation. Even when things weren't going my way, you always helped me keep my chin up. This thesis is a culmination of my undergraduate career at MIT, and I would not be at the finish line without you.

Table of Contents

List of Figures

1 Introduction

In 2006, John Pendry and his colleagues at Duke University demonstrated to the world something only thought of to exist in the lore of science fiction and fantasy: an invisibility cloak. The cloak deflected microwave beams so they flew around a "hidden" object inside with little distortion, making it appear almost as if nothing were there at all. The researchers manufactured the cloak using optical metamaterials, nano-scale structures precisely arranged in a manner that caused microwaves to flow around the cloaked object in the same way that water would [1]-[2].

Optical metamaterials are artificially engineered materials with exceptional electromagnetic properties that cannot be found in nature. Because of the immense control they provide over the propagation of light, metamaterials have driven forward many fields including sensing and imaging, telecommunications, medical diagnostics, and solar energy harvesting over the last 20 years. Unlike naturally occurring optical materials which achieve their properties from their composition on the atomic scale, metamaterials achieve their properties from their carefully designed microscale and nanoscale structures. By tuning the shape, geometry, orientation, and arrangement of these structures, unconventional optical properties can be achieved over a broadband wavelength range of operation.

Metamaterials are composed of structural elements that are of sub-wavelength scale, which means their dimensions are relatively small compared to the operating wavelength of light, and yet much larger than atomic or molecular length scales. These elements, or “meta-atoms”, are often periodically arranged metal-dielectric composites, and they take on the role of atoms in a natural material [3].

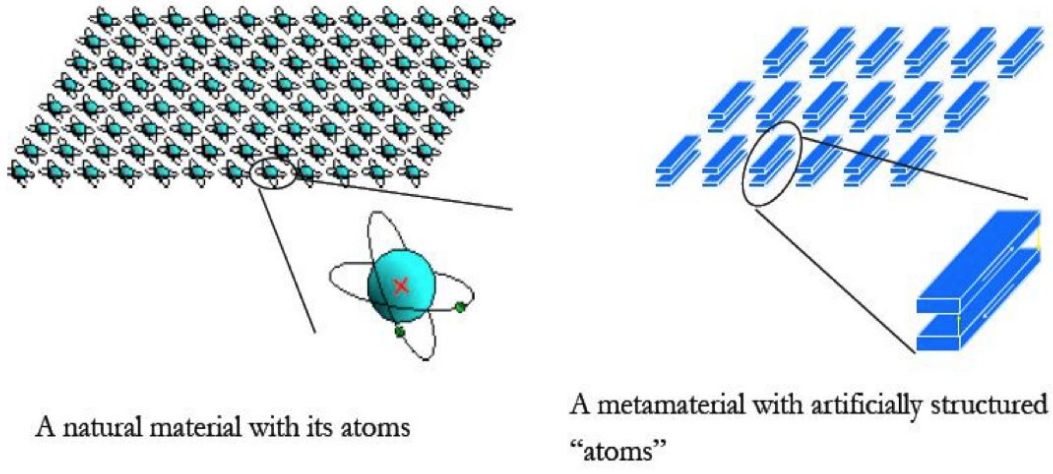

Figure 1: An illustration of a natural material and a metamaterial provided by [3]

Like a crystal at length scales beyond the atomic, metamaterials can be treated as homogeneous media at length scales beyond that of the constituent meta atoms, characterized with spatially-averaged effective dielectric parameters that characterize the metamaterial's optical modulation properties under certain criteria.

2 Objectives and Motivation

The goal of this project is to theoretically investigate the optical performance of $Ge_2Sb_2Te_5$ (GST)-based uniaxial, anisotropic metamaterial designs, namely nanolayered and nanowired metamaterials, in the near-infrared (nIR). This project is undertaken in collaboration with the Advanced Materials and Microsystems Group at MIT Lincoln Laboratory. The Advanced Materials and Microsystems Group is interested in investigating broadband wavelength regions of (1) high reflectance contrast between the amorphous and crystalline GST states, (2) high birefringence and (3) zero-crossing birefringence for future integrated photonic devices operating in the nIR. Thus, this simulative work aims to serve as a theoretical precursor to experimental nanofabrication of GST-based optical devices.

The field of infrared optics is one which remains reliant on bulky, high cost, and often high loss system components compared to those operating in the visible light spectrum [12]. Thus, high reflectance contrast, high birefringence, and zero-crossing birefringence are chosen as figures of merit for the optical performance of the GST-based metamaterial designs because optimizing these parameters can improve the size, weight, power consumption, and cost of photonic devices. For example, in photonic devices that rely on switching technology, like optical gates in telecommunication networks and optical data storage systems, maximizing the reflectance contrast of core device materials can be an important step towards increasing their compactness and energy efficiency [11]. In polarization-modulative devices like holograms and liquid crystal displays, that take advantage of the constituent material's birefringence, increased birefringence can allow optical devices to achieve the same induced phase shift between polarization modes at a smaller material dimension, decreasing device size and cost. Finally, investigation into zero-crossing birefringent materials can increase the broadband range of operation of narrow bandpass filters like Lyot filters, allowing for very low-loss light transmission and reducing the number of components necessary to attain a set of spectral bands.

In order to achieve the above three optical properties of interest, GST, a phase change material, is selected as the simulative alloy of choice due to its fast switching speeds, high metastability, high reflectance contrast between states, scalable optical properties, and widespread usage as a

core material in many optical data storage systems [10]. When repeatedly cycled, compositional and structural deviations as a result of tellurium migration can cause large fluctuations in the electrical resistance of the amorphous and crystalline GST states. This drift creates noise and prevents GST from usage in high precision-based computing applications like neuromorphic computing. In order to mitigate this drift, silicon dioxide (SiO_2) is proposed and selected as a confinement dielectric to co-compose the two-component metamaterial designs due to its adherence to criteria outlined in [10]. Additionally, air is used as another dielectric to co-compose the metamaterial with GST . The refractive index *n* and extinction coefficient *k* values for crystalline and amorphous GST and SiO_2 can be found in the Appendix.

Effective medium theory (EMT) is used to homogenize the GST-SiO_2 and GST-air metamaterials and calculate effective dielectric parameters used to calculate the above figures of merit. Additionally, the propagation of light through each metamaterial is simulated using a transfer matrix method (TMM) on the metamaterial as designed and as a homogenized layer.

3 Theoretical Background and Methods

3.1 Effective Medium Theory of Anisotropic Metamaterials

In traditional optical materials, dielectric response to light is primarily due to the polarization of atoms. However, the optical properties of metamaterials are characterized by the interaction of light with meta-atoms. On the microscopic scale (meta-atomic scale and smaller), electric fields are strongly inhomogeneous and have to be determined by solving for the interaction of electromagnetic fields with each individual meta-atom. But a macroscopic electric field *E* and polarization *P* can be introduced as a result of spatially averaging local microscopic electric fields and local dipole moments over large groups of meta-atoms. This can be achieved provided that the incident radiation has a wavelength that is much larger compared to the size of the meta-atoms.

Under this criteria, the defined average fields can be considered homogenous within the metamaterial and the idea of a homogeneous dielectric medium with an effective permittivity can be introduced. This effective dielectric permittivity, ε_{eff}, can be calculated from the ratio between the spatially-averaged displacement field <D> and the spatially-averaged electric field <E>, where the brackets indicate averaging over the microscopically large (multiple meta atoms), macroscopically small (subwavelength) spatial area :

$$< D > = \varepsilon_{eff} < E > \quad (1)$$

The effective permittivity is completely determined by the weighted averaged characteristics of the metamaterial's constituents, including average meta-atom shape, average meta-atom concentration, and average meta-atom arrangement [4]. Note that in general, the effective permittivity is a tensor quantity. Two metamaterial designs that possess anisotropic effective permittivity tensor properties are uniaxial nanolayered and nanowired structures.

3.1.1 Nanolayered Metamaterials

Let's consider the effective permittivity of a multilayered periodically arranged stack made from isotropic constituent materials with permittivities ε_i and layer thicknesses d_i, illustrated in Figure 2.

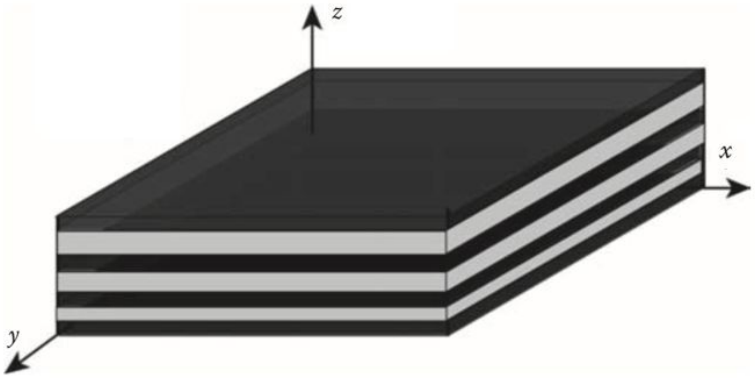

Figure 2: An illustration of a uniaxial nanolayered metamaterial provided by [4]

For a uniaxial stack, the effective permittivity tensor is a diagonal matrix that can be written as :

$$\varepsilon_{eff} = \begin{bmatrix} \varepsilon_x & 0 & 0 \\ 0 & \varepsilon_y & 0 \\ 0 & 0 & \varepsilon_z \end{bmatrix} = \begin{bmatrix} \varepsilon_{\parallel} & 0 & 0 \\ 0 & \varepsilon_{\parallel} & 0 \\ 0 & 0 & \varepsilon_{\perp} \end{bmatrix} \quad (2)$$

Where $\varepsilon_{\parallel}$ is the permittivity component in the plane of the layers (in the x-y plane) and $\varepsilon_{\perp}$ is the permittivity component out of the plane of the layers (along the z axis). Equation 1 yields the uniaxial anisotropic effective permittivity with diagonal components of the permittivity tensor being

$$\varepsilon_{\parallel} = \frac{\sum d_i \varepsilon_i}{\sum d_i} \quad (3.1)$$

$$\varepsilon_{\perp} = \frac{\sum d_i}{\sum d_i/\varepsilon_i} \tag{3.2}$$

For a two-component multilayer stack, Equations 3.1 and 3.2 reduce to:

$$\varepsilon_{\parallel} = \frac{d_1\varepsilon_1 + d_2\varepsilon_2}{d_1 + d_2} = f\varepsilon_1 + (1-f)\varepsilon_2 \tag{4.1}$$

$$\varepsilon_{\perp} = \frac{\varepsilon_1\varepsilon_2(d_1 + d_2)}{d_1\varepsilon_2 + d_2\varepsilon_1} = \frac{\varepsilon_1\varepsilon_2}{f\varepsilon_2 + (1-f)\varepsilon_1} \tag{4.2}$$

It is important to note that the properties of the homogenous slab are no longer controlled by individual sizes of meta atoms (d_1 and d_2) but by their relative concentrations or fill fraction *f,* where $f = d_1/(d_1 + d_2)$ [4]. However, we must still remain in the effective medium regime in order for ε_{eff} to remain valid.

3.1.2 Nanowired Metamaterials

A similar formalism can be followed to attain $\varepsilon_{\parallel}$ and $\varepsilon_{\perp}$ for a nanowired metamaterial. This structure is based on arrays of aligned nanoscale wires of permittivity ε_i deposited with radius *R* in a dielectric matrix with ε_h (Figure 3). Unlike in nanolayered metamaterials, where the fill fraction is characterized by the thicknesses of the constituent layers, in nanowired metamaterials the cross sectional area of the nanowires and the interwire distance *a* define the fill fraction *f*, where $f = \pi R^2/a^2$ [4]. For this geometry, Equation 1 yields:

$$\varepsilon_{\parallel} = f\varepsilon_1 + (1-f)\varepsilon_2 \tag{5.1}$$

$$\varepsilon_{\perp} = \frac{2f\varepsilon_1\varepsilon_2 + (1-f)\varepsilon_2(\varepsilon_1 + \varepsilon_2)}{2f\varepsilon_2 + (1-f)(\varepsilon_1 + \varepsilon_2)} \tag{5.2}$$

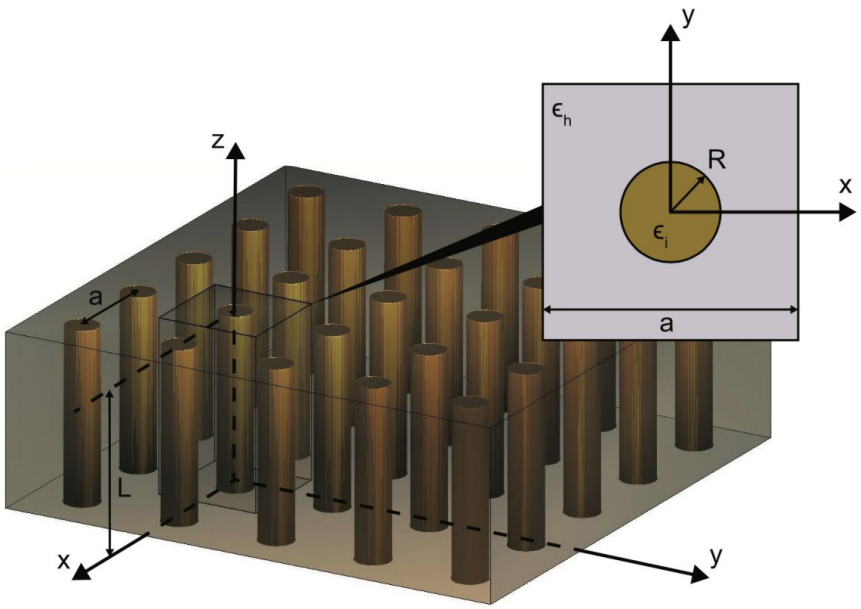

Figure 3: An illustration of a uniaxial nanowired metamaterial provided by [18]

3.2 Form Birefringence

Optical birefringence, or double refraction, is an important optical property that has played a key role in the development of many modern optical devices, such as holograms, light modulators, liquid crystal displays, and wave plates [5]. Optical birefringence anisotropically generates phase retardation for optical waves, resolving an incident light wave into two orthogonal linear polarization modes (transverse electric (TE), in which the electric field is parallel to the plane of incidence and transverse magnetic (TM), in which the electric field is perpendicular to the plane of incidence) and producing a phase shift between them.

Birefringence appears in natural optical materials, most visibly in the double images formed by non-cubic crystals like calcite and quartz. But in periodic metamaterials with different constituent dielectric media, optical birefringence can also be induced. This is known as form, or artificial, birefringence. For a uniaxial anisotropic metamaterial as described in Section 3.1, each polarization mode "feels" a different refractive indices, n_e and n_o, the extraordinary and ordinary refractive indices [6]. Under the same coordinate system defined in Section 3.1, $n_e = \varepsilon_{\perp}^{1/2}$ and $n_o = \varepsilon_{\parallel}^{1/2}$. Thus, form birefringence can be calculated as $\Delta n = \text{Real}\,(n_e - n_o)$, Furthermore, the induced optical path difference (retardation) between the polarization modes is given by $\Phi = 2\pi \Delta n\, d/\lambda$, where d is the total thickness of the material and λ is the wavelength of incident light

[7]. Because birefringence is wavelength dependent, there sometimes exist wavelength regimes where there is no difference between the extraordinary and ordinary refractive indices, where $\Delta n = 0$ and the material behaves isotropically. These regimes are known as zero-crossings, and they can be used to filter narrow bands of light with little to no loss of signal.

3.3 Transfer Matrix Method and Reflectance

In addition to understanding retardation, it is also of great interest to know in what manner light propagates through a metamaterial over a broadband wavelength range of operation; in other words, across what wavelength regimes light is allowed to transmit though or be reflected by the metamaterial. In general, the propagation of light through various media can be considered in terms of transfer matrices and the transfer matrix method (TMM).

Let's first consider a tri-layered metamaterial with indices n_1, n_2, and n_3 and thicknesses d_1, d_2, and d_3 respectively. While propagating through the stack, the light is always behaving in one of three ways: (1) transferring between layers, (2) propagating forward within a layer, (3) or propagating backwards within a layer due to reflection at a layer-layer interface. These behaviors and their effect on the components of the electric field of the incident light can be described sequentially using matrices.

If we assume light behaves as a monochromatic plane wave and propagates in the x-direction then for TE polarized light, the electric fields in each layer can be represented as:

$$E_1 e^{ik_1 x} + E_1' e^{-ik_1 x} \qquad \text{for x} < d_1$$

$$E_2 e^{ik_2 x} + E_2' e^{-ik_2 x} \qquad \text{for x } d_1 < \text{x} < d_2$$

$$E_3 e^{ik_3 x} + E_3' e^{-ik_3 x} \qquad \text{for x } d_2 < \text{x} < d_3$$

Where E_1, E_2, and E_3 are the amplitudes of components of the electric field propagating forwards and E'_1, E'_2, and E'_3 are the amplitudes of the reflected components propagating backward. In order to relate the electric field amplitudes in the first layer to the third layer, we will have to consider propagation through layer 1, across the layer 1-layer 2 interface, through layer 2, and across the layer 2- layer 3 interface. By taking the input wave amplitude components of the incident and reflected light (forward and backward propagating amplitudes) as a 2 x1 vector, for each interface encountered a 2 x 2 transfer matrix is applied to the input amplitude vector, and for each medium of thickness d_i the light propagates through, a 2 x 2 propagation matrix is

applied. From this matrix multiplication, we can eventually determine the reflection and transmission coefficients of the stack [8].

The 2 x 2 propagation matrix accounts for the accumulation in phase of a plane wave as it propagates through a layer and is given generally as P_i

$$P_i = \begin{bmatrix} e^{2\pi i n_i cos(\Theta) d_i/\lambda} & 0 \\ 0 & e^{-2\pi i n_i cos(\Theta) d_i/\lambda} \end{bmatrix} \tag{6}$$

For transfer of light between two layers, $T_{i\text{-}i+1}$ represents the transfer from layer i to layer i+1 and for TE polarized light, it is given as:

$$T_{i-i+1} = \begin{bmatrix} \frac{n_{i+1}cos(\Theta_{i+1})+n_i cos(\Theta_i)}{2n_{i+1}cos(\Theta_{i+1})} & \frac{n_{i+1}cos(\Theta_{i+1})-n_i cos(\Theta_i)}{2n_{i+1}cos(\Theta_{i+1})} \\ \frac{n_{i+1}cos(\Theta_{i+1})-n_i cos(\Theta_i)}{2n_{i+1}cos(\Theta_{i+1})} & \frac{n_{i+1}cos(\Theta_{i+1})+n_i cos(\Theta_i)}{2n_{i+1}cos(\Theta_{i+1})} \end{bmatrix} \tag{7}$$

Using these propagation and transfer matrices, the electric field amplitudes in layer 1 and layer 3 can be related through matrix multiplication as

$$T_{23}P_2T_{12}P_1 \begin{bmatrix} E_1 \\ E_1' \end{bmatrix} = M \begin{bmatrix} E_1 \\ E_1' \end{bmatrix} = \begin{bmatrix} E_3 \\ E_3' \end{bmatrix} \tag{8}$$

The ratio between M_{21} and M_{11} gives the reflection coefficient r_{TE}, which can be used to find the reflectance, $R_{TE} = r_{TE}^2$. In this paper, we'll restrict our cases of light incidence to normal incidence (Θ_1= 0 degrees), so the reflectance of the TE and TM modes becomes redundant and $R_{TE} = r_{TE}^2 = R_{TM}$

3.4 Phase Change Materials

Another axis with which to further control the flow of light in metamaterials is through tunability in the constituent materials' dielectric constants. One class of materials that provides this tunability is phase change materials. Phase change materials (PCMs) are materials that exist in at least two structurally unique metastable solid phases, an amorphous phase and at least one crystalline phase. Typically, the amorphous and crystalline phases(s) have very different optical and electrical properties, due to large differences in structure and bonding between the phases. It is possible to switch between these phases on nanosecond time scales using joule heating. The transformation from the amorphous phase to the crystalline phase occurs by heating the material

above its crystallization for a time long enough for crystallization to occur using a low current laser pulse. This pulse is known as the SET pulse. The reverse transformation, from the crystalline to the amorphous phase, occurs by heating the material above its melting temperature using a higher current laser pulse and rapidly quenching it. This pulse is known as the RESET pulse [9]. Depending on the particular crystallization kinetics of the PCM as well as the parameters of the laser pulse during joule heating, a range of dielectric constants can be achieved as the PCM transitions between its low refractive index amorphous and high refractive index crystalline states. When used as a constituent of a metamaterial, this provides even more control over optical modulation.

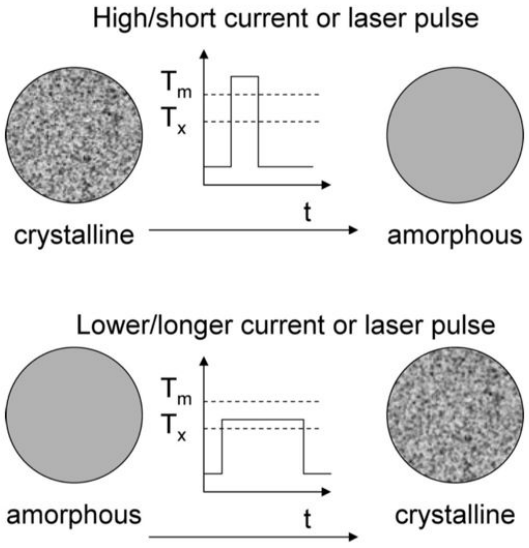

Figure 4: A schematic of the RESET (a) and SET (b) pulses, with T_m and T_x as the crystallization temperature provided by [9]

The $Ge_2Sb_2Se_xTe_{1-x}$ family of chalcogenide alloys has been extensively investigated as phase change materials. In this paper, $Ge_2Sb_2Te_5$ (GST) is of the Ge-Sb-Te system is selected as the simulative PCM of choice due to its fast switching speeds, high metastability, high optical contrast between states (see Appendix), scalable optical properties, and widespread usage as a core material in many optical data storage systems [10]. In this family, GST is considered to be the 'grandfather material' and is therefore well characterized and well understood. That being said, GST's high extinction coefficient in both states leads to optical losses during extensive cycling, placing a lower limit on the potential of its optical performance

4 Results and Discussion

Both EMT and TMM analysis were performed using validated, homemade code written in MATLAB by Dr. Christopher Roberts in the Advanced Materials and Microsystems Group at MIT Lincoln Laboratory. This code has been thoroughly tested against many edge cases and used in published literature [15]-[17]. As a further check, personal TMM code was also written and produced initial results consistent with that of Dr. Roberts' code. Here, the reflectivity and form birefringence of nanolayered and nanowired GST-SiO_2 and GST-air metamaterial designs in the near infrared are discussed.

4.1 Fundamental Analysis with EMT and TMM

For initial fundamental analysis, the limits of effective medium theory when compared to the transfer matrix method were investigated. Unlike EMT, TMM imposes no limits on the structural scale of the metamaterial when compared to the operating wavelength. Thus, reflectance simulations were performed for both a nanolayered GST-SiO_2 structure and a subsequently homogenized structure using TMM. When performing these initial TMM-EMT comparisons, the thickness of the SiO_2 layers was fixed at 5 nanometers and the thickness of the GST layers was varied. In the effective medium regime ($d << \lambda$), the reflectance values for the nanolayered and homogenous layer metamaterial were consistent with each other until $f \sim 0.9$. Thus, in addition to the initial constraint of remaining in the effective medium regime, all further nanolayered EMT calculations taken at $f > 0.9$ were considered invalid.

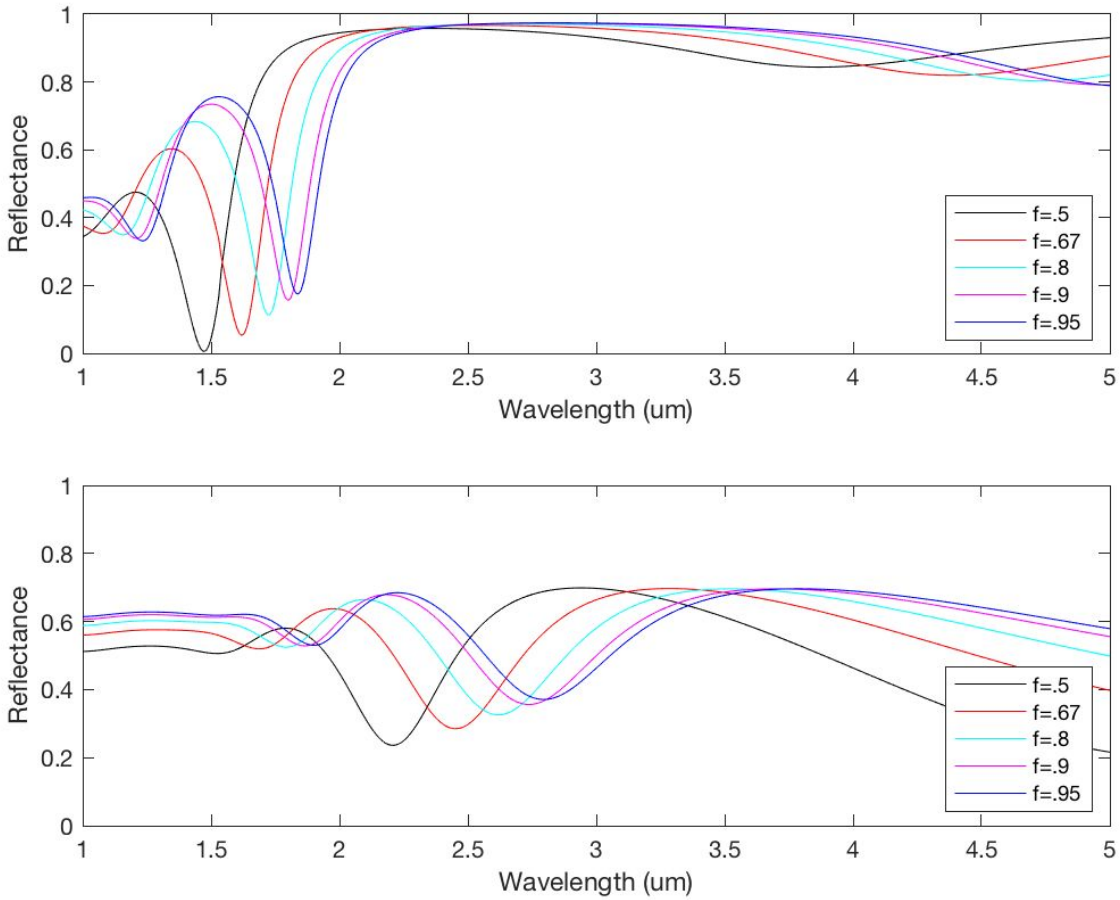

Figure 5. (a) The reflectance spectrum of the amorphous GST-SiO_2 homogenous layer with a thickness of 300 nm at various fill fractions. (b) The reflectance spectrum of the crystalline GST-SiO_2 homogenous layer with a thickness of 300 nm at various fill fractions

The relationship between the fill fraction and the reflectance spectrum of a homogenized GST-SiO_2 nanolayered structure was also investigated, as shown in Figure 5. Figure 5a and 5b demonstrate the reflectance spectrum of a 300 nanometer thick homogenized GST-SiO_2 structure in the high reflectance amorphous-SiO_2 and low reflectance crystalline-SiO_2 states respectively at various fill fractions of GST. The results indicate that for a fixed homogenous layer thickness, reflectance minima and maxima for both amorphous and crystalline GST-SiO_2 redshift and increase, but additionally broaden in the crystalline- state, with increasing fill fraction. This insight into the effect of fill fraction on the reflectance spectrum can allow for more predictable control over the reflectance properties of GST-based devices in the nIR.

4.2 Reflectance Analysis

The GST metamaterials were investigated for high reflectance contrast resulting from switching in broadband wavelength regimes in the nIR. Due to the large difference in optical properties of the constituent GST amorphous and crystalline phases, a region of high reflectance contrast was evident in both the nanolayered and nanowired GST-SiO_2 and GST-air structures.

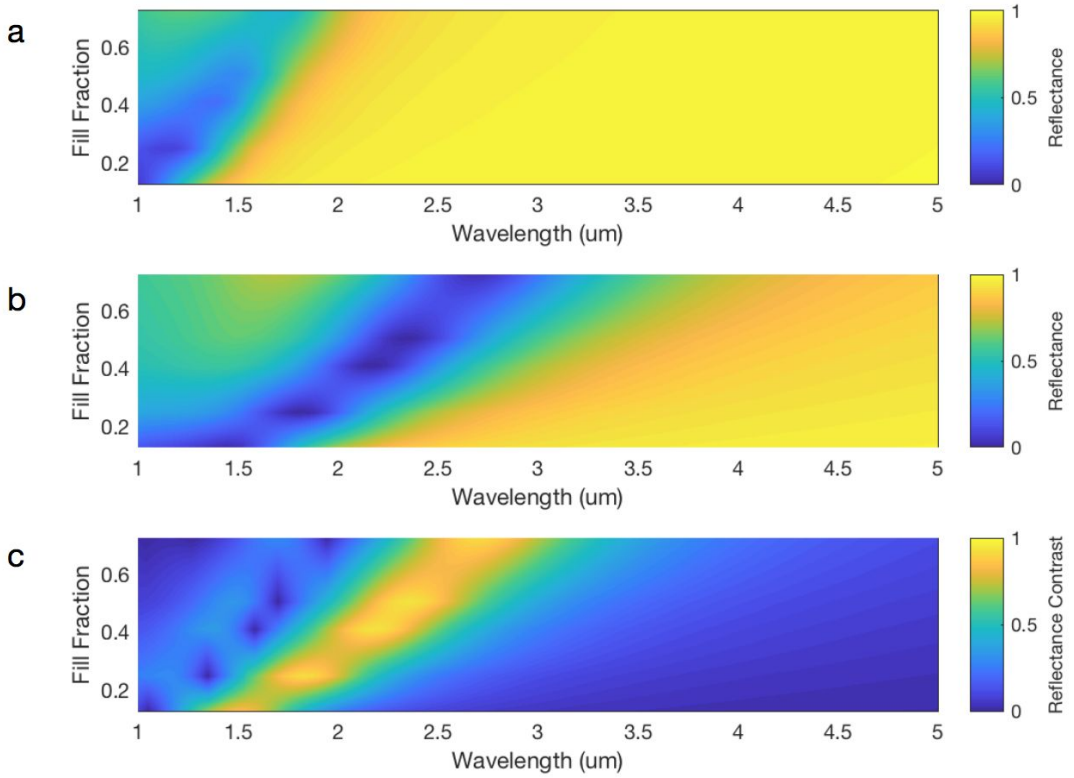

Figure 6. (a) The reflectance spectrum of the amorphous nanowired GST-SiO_2 with a thickness of 100 nm as a function of fill fraction. (b) The reflectance spectrum of the crystalline nanowired GST-SiO_2 with a thickness of 100 nm as a function of fill fraction. (c) The absolute value of the difference in reflectance between the two GST states in (a) and (b) as a function of fill fraction

Figure 6 illustrates a set of surface plots of the reflectance spectrum of the amorphous (a) and crystalline (b) states as well as the reflectance contrast between the two states (c) of a 100 nanometer thick nanowired GST-SiO_2 structure plotted as a function of GST fill fraction. Here, the reflectance contrast is given as the absolute value of the difference between the reflectance of the amorphous state and crystalline states. Between 1.25 microns and 3 microns, there exists a large region of high reflectance contrast between the amorphous and crystalline states (Figure 6c). Within this region, the reflectance contrast varies between 70% and 95% with the maximum reflectance contrast occuring at $f = 0.4$ and $\lambda = 2.2$ microns. This maximum reflectance contrast

is nearly 15 % higher than that of the maximum reflectance contrast found in the same wavelength regime of a GST thin film with similar thickness [13]. This enhanced reflectance contrast can most likely be attributed to the nanowired metamaterial design.

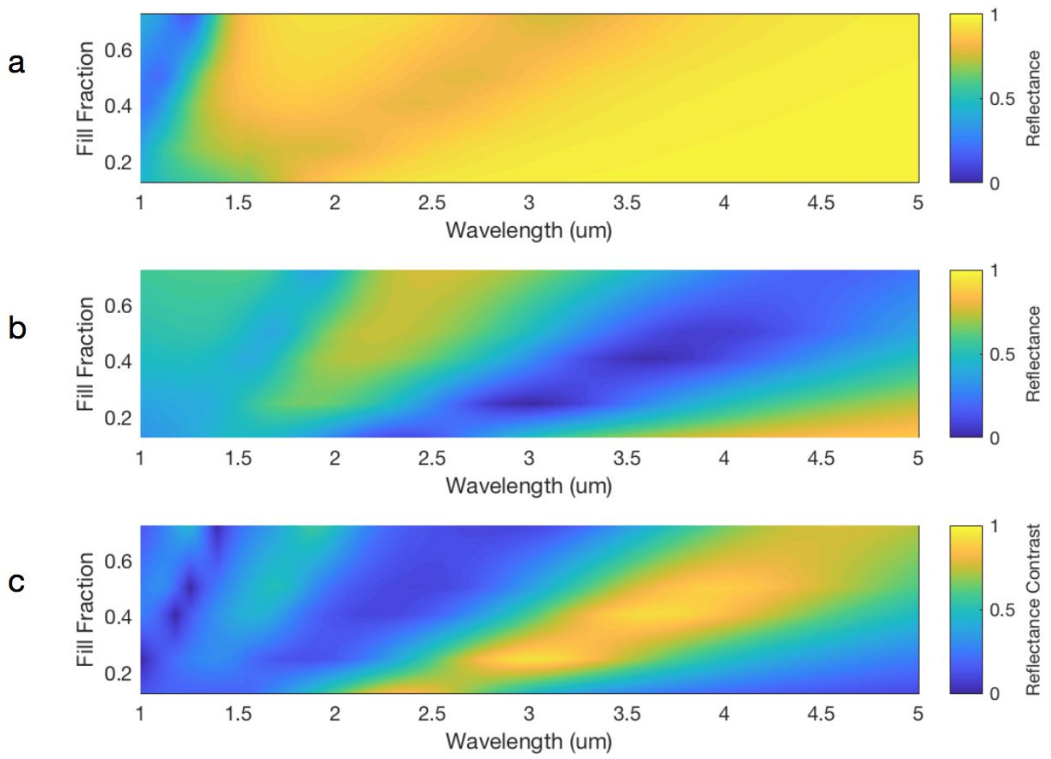

Figure 7. (a) The reflectance spectrum of the amorphous nanowired GST-SiO_2 with a thickness of 200 nm as a function of fill fraction. (b) The reflectance spectrum of the crystalline nanowired GST-SiO_2 with a thickness of 200 nm as a function of fill fraction. (c) The absolute value of the difference in reflectance between the two GST states in (a) and (b) as a function of fill fraction

When the total thickness of the nanowired structure is doubled to 200 nanometers (Figure 7), this region of high reflectance contrast redshifts and broadens to a wavelength regime of 2 microns to 4.5 microns (Figure 7c). In this region, the range of reflectance contrast values slightly decreases to between ~70% to 90%. Further simulations show that with increasing metamaterial thickness, this region of high reflectance continues to broaden and redshift. Additionally, the maximum reflectance contrast decreases while the minimum reflectance contrast increases with increasing metamaterial thickness. These results demonstrate that in addition to fill fraction, metamaterial thickness can be used to tune reflectance properties in the nIR.

4.3 Form Birefringence Analysis

Form birefringence for the TE and TM modes was also evaluated for the above nanolayered and nanowired metamaterials as a function of fill fraction. Preliminary analysis showed that birefringence minima (highest magnitude birefringence) were consistently found between 1 and 1.6 microns regardless of metamaterial geometry or GST state. This birefringence resonance can most likely be attributed to the low wavelength behavior of the refractive index of the constituent GST phases (see Appendix) and should be further investigated in future work.

The metamaterials with the highest magnitude birefringence were the crystalline GST composites due to the high refractive index of the constituent crystalline GST state in the nIR. Figure 8 shows a surface plot of the form birefringence of a nanolayered crystalline GST-air metamaterial as a function of fill fraction. This metamaterial exhibits a large region of high birefringence Δn on the order ~ 4 - 5 between 1.2 and 2 microns over a large fill fraction range. In this region exists a maximum birefringence of 5 at λ= 1.5 microns and f = 0.8 . Nematic liquid crystals, a commonly used polarization-modulative material, have a birefringence on the order of Δn = 0.2 [14]. Here, we present a metamaterial with a maximum birefringence 25 times larger than that of a state of the art birefringent material.

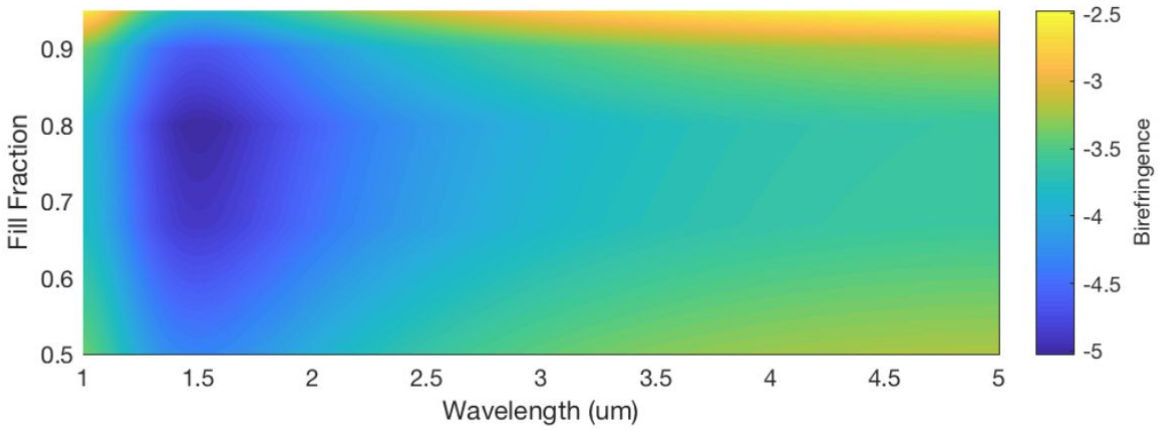

Figure 8. The form birefringence of nanolayered crystalline GST- air as a function of fill fraction

When nanolayered crystalline GST-air is switched to the amorphous state (Figure 9), the metamaterial exhibits a region of high birefringence on the order ~ 1.8- 2.4 between 1 micron and 1.5 microns over a similarly large fill fraction range. This is a birefringence over 10 times higher than that of nematic liquid crystals. If gradually switched through partially crystalline-partially amorphous GST states, the high birefringence contrast of ~2.2- 2.6 between the two metastable GST states in this low wavelength regime can be utilized. For example, such control of a high birefringence range can be used to increase the conversion efficiency of

photovoltaic solar cells, the resolution of nIR sensing devices, and the power efficiency of telecommunication networks.

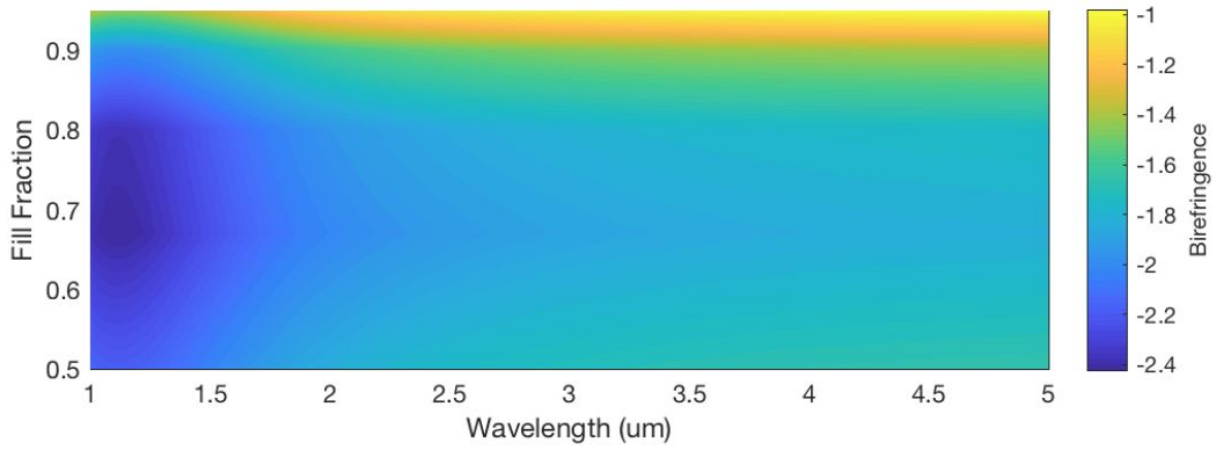

Figure 9. The form birefringence of nanolayered amorphous GST- air as a function of fill fraction

Regions of zero-crossing birefringence were also investigated. Figure 10 is a surface plot of the form birefringence of a nanolayered crystalline-GST-amorphous GST metamaterial as a function of fill fraction. At $f = 0.9$ and between $\lambda = 1$ micron and $\lambda = 1.1$ microns exists a zero birefringence regime. One immediate drawback of this metamaterial is the high fill fraction needed to produce zero birefringence, which could pose as a cost barrier to implementation in optical filters. In the future, zero-crossings at lower fill fractions will be explored for this metamaterial.

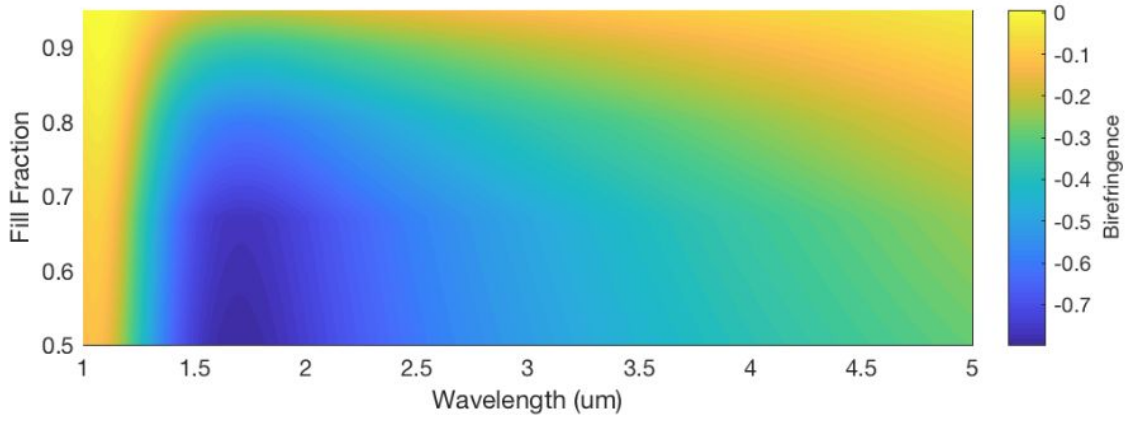

Figure 10. The form birefringence of nanolayered crystalline GST- amorphous GST as a function of fill fraction.

5 Conclusion and Future Work

We theoretically investigated the optical performance of GST-based nanolayered and nanowired metamaterials. To do this, high reflectance contrast, high birefringence, and zero-crossing birefringence were established as figures of merit and effective medium theory and transfer matrix method analyses were used to calculate them. It was shown that both GST-based nanolayered and nanowired metamaterials can exhibit broadband high reflectance contrast on the order of 95% over a wavelength range of over 1.5 microns in the near infrared. Furthermore, the bandwidth and location of this high reflectance contrast region can be tuned using metamaterial thickness and fill fraction. This high reflectance contrast metamaterial can have direct applications in improving switching based technologies, like optical gates, tunable near infrared shutters, and optical data storage systems.

Additionally, we presented a GST-air nanolayered metamaterial possessing a form birefringence 25 times larger than that of state of the art liquid crystals. Because birefringence is proportional to the induced phase shift, this metamaterial can be used to decrease the size and weight of polarization-modulative devices. Finally, a zero-crossing birefringent region was found in a nanolayered crystaline GST-amorphous GST metamaterial, but more simulations at lower fill fractions are necessary for this to be viable for usage as a zero-crossing birefringent material.

This simulative work aims to serve as a theoretical precursor to experimental nanofabrication of GST-based optical devices. The next step would be to sputter the above metamaterials, test their reflectance and birefringence properties, and compare the results to simulation. In parallel, further questions of metamaterial design and composition should be explored. In this work, intrinsically isotropic materials were used to generate metamaterial anisotropy. It has been demonstrated in [6] that intrinsically birefringent materials incorporated with intrinsically isotropic materials in a metamaterial can generate unique birefringent properties. Thus, combining the above simulative GST-based metamaterials with GST or another isotropic dielectric or PCM could provide further tunability of the metamaterial's birefringent properties. Additionally, the influence of more complex unit cell geometries like embedded nanospheres or elliptical nanowires on the metamaterial's reflectance and birefringence should be investigated.

Despite exhibiting excellent optical contrast, fast switching speeds, and high metastability, the performance of GST is limited by its high extinction coefficient contrast between its states, often leading to losses during cycled switching. One more recent family of optical PCMs that shows promise for usage in metamaterial designs is the Ge-Sb-Se-Te family [19]. In particular, $Ge_2Sb_2Se_4Te_1$ (GSST) is being investigated due to its good optical contrast and low extinction coefficient contrast, with an especially low extinction coefficient in its amorphous state (see Appendix). GSST exhibits much lower optical losses in its states compared to many standard

optical phase change materials, including GST. Given its lower loss states and smaller optical contrast well throughout the IR as compared to GST, GSST-based optical metamaterials may exhibit zero-crossing birefringence more prominently over a broadband wavelength range of operation.

Despite this promise, its performance endurance over an extensive lifetime has yet to be demonstrated, and more work needs to be done in order for GSST to be viable for widespread implementation in switching-based technologies. Thus, the TMM and EMT analyses on GST-based optical metamaterials should be repeated using GSST . Similar regions of high reflectance, high birefringence, and zero-crossing birefringence should be investigated using the results achieved by GST in this paper as optical performance metrics.

6 References

[1] “First Demonstration of a Working Invisibility Cloak.” *Duke Pratt School of Engineering*, 1 Mar. 2018, pratt.duke.edu/about/news/first-demonstration-working-invisibility-cloak.

[2] “Refractive Properties of Photonic Crystals and Metamaterials.” *Photonic Crystals*, pp. 197–223., doi:10.1007/978-3-540-78347-3_6.

[3] Trivedi, Ranjana et al. “Metamaterial: Materials with Exceptional Properties.” (2018).

[4] Noginov, Mikhail A., and Viktor A. Podolskiy. *Tutorials in Metamaterials*. CRC Press, 2016.

[5] Zhang, Wenfu, and Wei Zhao. “Birefringence in Photonic Crystal Structures: Toward Ultracompact Wave Plates.” *Advances in Photonic Crystals*, 2013, doi:10.5772/55142.

[6] Emoto, Akira, et al. “Form Birefringence in Intrinsic Birefringent Media Possessing a Subwavelength Structure.” *Applied Optics*, vol. 49, no. 23, 2010, p. 4355., doi:10.1364/ao.49.004355.

[7] Yeh, Pochi. “Electromagnetic Propagation in Birefringent Layered Media.” *Journal of the Optical Society of America*, vol. 69, no. 5, 1979, p. 742., doi:10.1364/josa.69.000742.

[8] “Layered Materials and Photonic Band Diagrams.” *https://ocw.mit.edu*, 2013.

[9] Raoux, Simone, et al. “Phase Change Materials and Their Application to Nonvolatile Memories.” *Chemical Reviews*, vol. 110, no. 1, 2009, pp. 240–267., doi:10.1021/cr900040x.

[10] Ding, Keyuan, et al. “Phase-Change Heterostructure Enables Ultralow Noise and Drift for Memory Operation.” *Science*, vol. 366, no. 6462, 2019, pp. 210–215., doi:10.1126/science.aay0291.

[11] Kawashima, Hitoshi, and Hiroyuki Tsuda. “Self-Holding Optical Switch Using Phase-Change Material for Energy Efficient Photonic Network.”

[12] Paschotta, Rüdiger. “Infrared Optics.” *RP Photonics Encyclopedia - Infrared Optics, Infrared Materials, Transparency, Broadband, Optical Properties, Coatings*, RP Photonics, 14 Mar. 2020, www.rp-photonics.com/infrared_optics.html.

[13] Sarangan, Andrew, et al. “Broadband Reflective Optical Limiter Using GST Phase Change Material.” *IEEE Photonics Journal*, vol. 10, no. 2, 2018, pp. 1–9., doi:10.1109/jphot.2018.2796448.

[14] Paschotta, Rüdiger. “Infrared Optics.” *RP Photonics Encyclopedia - Infrared Optics, Infrared Materials, Transparency, Broadband, Optical Properties, Coatings*, RP Photonics, 14 Mar. 2020, www.rp-photonics.com/infrared_optics.html.

[15] Roberts, Christopher, et al. “All Semiconductor Negative-Index Plasmonic Absorbers.” *Cleo: 2014*, 2014, doi:10.1364/cleo_qels.2014.fm1c.3.

[16] Wells, Brian M., et al. “Metamaterials-Based Salisbury Screens with Reduced Angular Sensitivity.” *Applied Physics Letters*, vol. 105, no. 16, 2014, p. 161105., doi:10.1063/1.4899131.

[17] Liu, Runyu, et al. “Enhanced Optical Transmission through MacEtch-Fabricated Buried Metal Gratings.” *Advanced Materials*, vol. 28, no. 7, 2015, pp. 1441–1448., doi:10.1002/adma.201505111.

[18] Wells, Brian M., et al. “Nonlocal Optics of Plasmonic Nanowire Metamaterials.” *Cleo: 2013*, 2013, doi:10.1364/cleo_qels.2013.qtu2a.2.

[19] Zhang, Yifei, et al. “Broadband Transparent Optical Phase Change Materials for High-Performance Nonvolatile Photonics.” *Nature Communications*, vol. 10, no. 1, 2019, doi:10.1038/s41467-019-12196-4.

7 Appendix

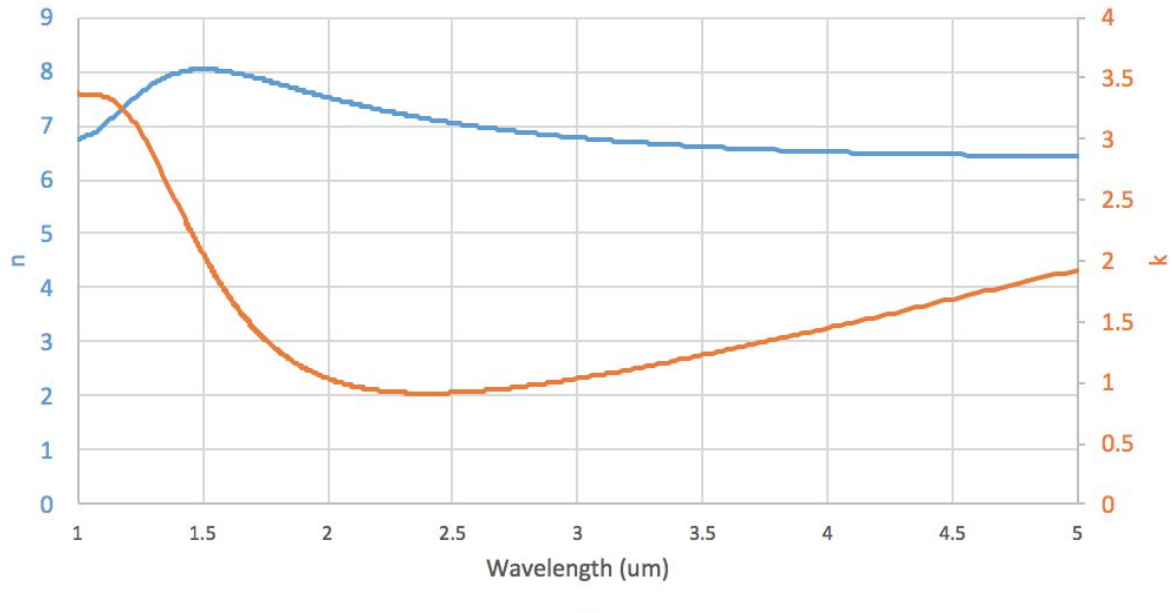

Figure A.1 The refractive index *n* (blue) and extinction coefficient *k* (orange) for crystalline GST

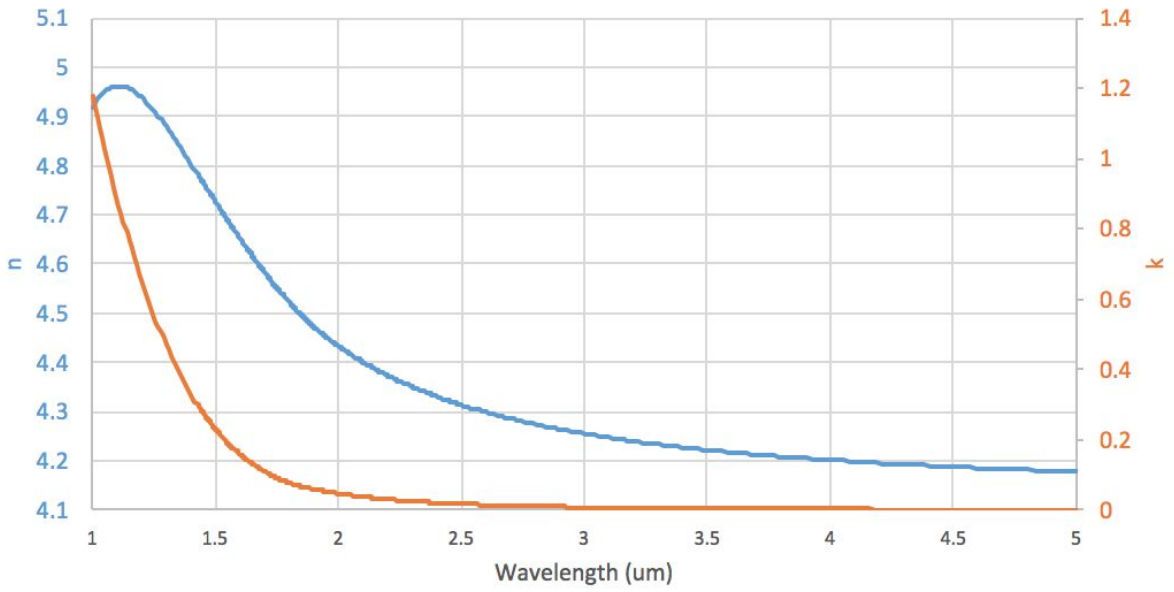

Figure A.2 The refractive index *n* (blue) and extinction coefficient *k* (orange) for amorphous GST

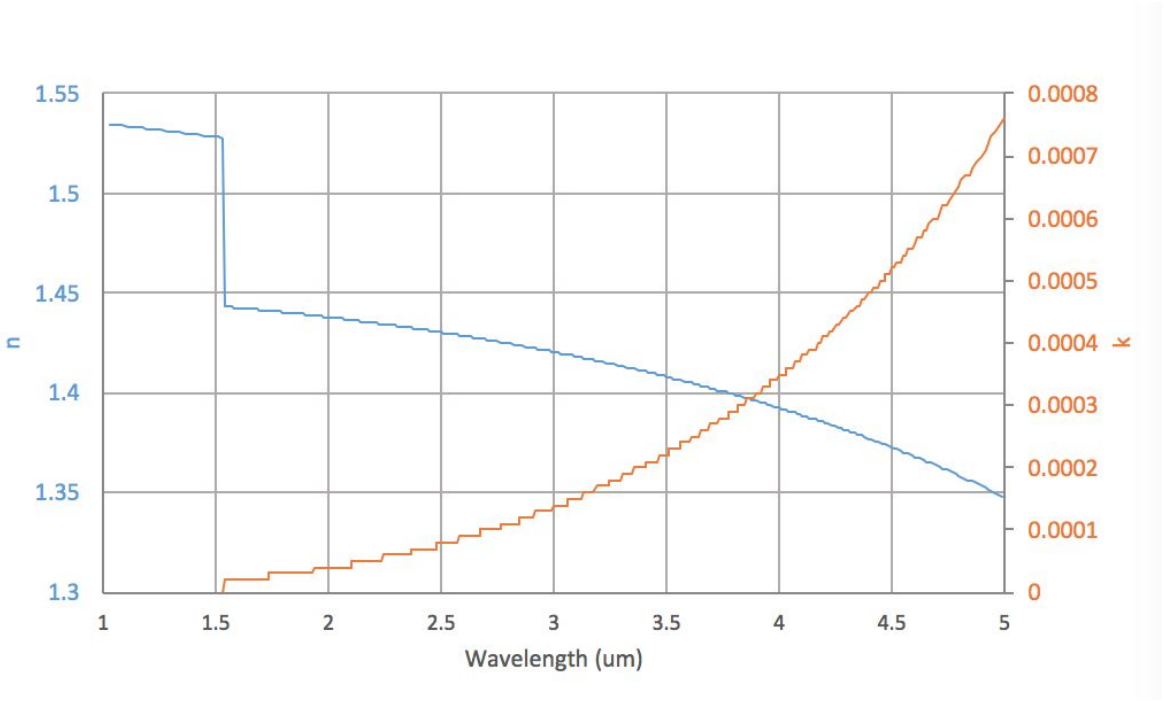

Figure A.3 The refractive index *n* (blue) and extinction coefficient *k* (orange) for silicon dioxide

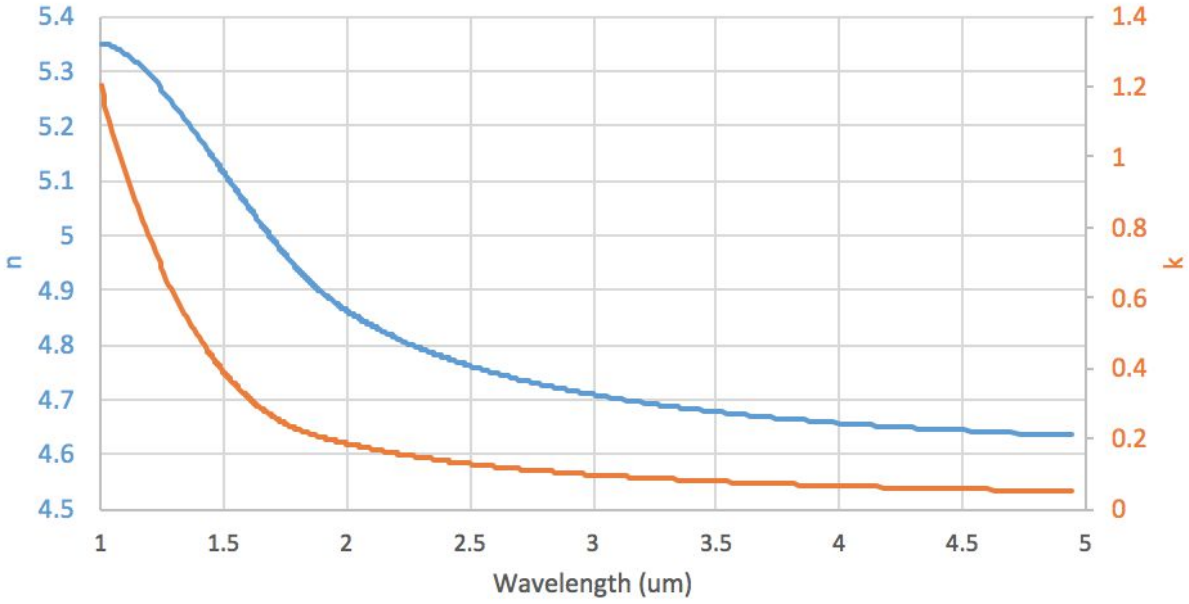

Figure A.4 The refractive index *n* (blue) and extinction coefficient *k* (orange) for crystalline GSST

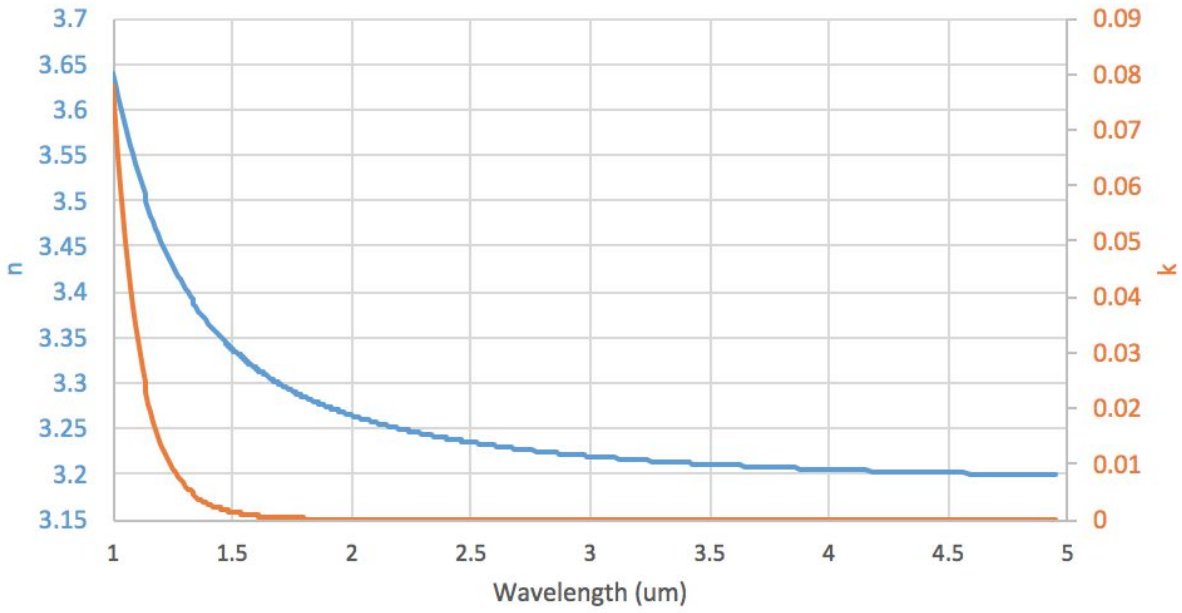

Figure A.5 The refractive index *n* (blue) and extinction coefficient *k* (orange) for amorphous GSST